

Geodetic investigation of transient deformation following the 2019 Ridgecrest earthquake sequence in southern California

Report for SCEC Award # 22069

Investigators: Roland Bürgmann (UCB), Eric Fielding (JPL), Zhen Liu (JPL), Kang Wang (UCB)

Other Participants: Niloufar Abolfathian (JPL)

Introduction

This project extends our previous effort in quantifying the spatial and temporal distribution of postseismic deformation during the first ~3.5 years after the 2019 Ridgecrest earthquake sequence. Additionally, this project explores the feasibility of extracting the north-south component of surface deformation along plate boundary and active faults using Multi-Aperture Interferometry (MAI) of Synthetic Aperture Radar (SAR) data.

Data

Built on our previous year's effort, we have now obtained a complete view of postseismic deformation ~3.2 years after the 2019 Ridgecrest earthquake mainshock using Sentinel-1 InSAR and GNSS observations (Figure 1). The original GNSS data used in this study are daily position time series at more than 400 continuous stations around the 2019 Ridgecrest rupture. The positions are in the International Terrestrial Reference Frame 2014 (ITRF2014) processed by the Central Washington University (CWU), archived at the Geodetic Facility for the Advancement of Geoscience (GAGE). We noticed that the original time series at a large portion of the stations exhibited sharp changes within a short duration (<5 days) that were not clearly documented in the published offset tables (e.g., the master steps database provided by the Nevada Geodetic Laboratory at the University of Nevada, Reno). Causes of such abrupt changes are not well understood, but could be sometimes attributed to a sudden change in the observation conditions (e.g., tree purges). Such offsets may affect the estimate of interseismic velocity at a given station, thus as a necessary step in the study of postseismic deformation, they must be corrected before the data can be used for further analysis. To tackle this problem, we first detrended the time series at each station between 2016 and 2022, and then visually inspected the 'flattened' time series to determine if there were any obvious short-duration changes during this time period. For each time epoch with apparent disruption, we estimated an offset by differencing the average positions 10 days before and 10 days after the corresponding offset time. To avoid overcorrection, we only applied the correction if the estimated offset were greater than 3 mm, which is roughly comparable to the scattering level of the original time series. The estimated offsets were then added back to the original time series to re-estimate the interseismic/preseismic deformation rate. To minimize the potential contamination due to the enduring postseismic relaxation from the 1992 Landers, 1999 Hector Mine and the 2010 El Mayor Cucapah earthquakes, the interseismic velocity at each station was estimated using data from only 3 years before the 2019 Ridgecrest earthquake.

Figure 1 shows the postseismic GNSS displacements at stations within 100 km from the 2019 Ridgecrest mainshock epicenter. The maximum horizontal displacement at the closest site P595 has reached more than 40 mm, 3 years after the mainshock. To characterize the spatial and temporal distributions of the observed displacement field, we performed a Principal Component Analysis (PCA) to the GNSS postseismic time series at stations within 100 km from the mainshock epicenter (Barbot et al., 2009; Dong et al., 2006). The results are shown Figure 1c and d. The temporal evolution of the horizontal component can be reasonably well approximated by a logarithm function $y = A \times \log(1 + \frac{t}{\tau})$ with a relaxation time $\tau \simeq 12.6$ days (Figure 1c). The overall improved fitting of the temporal evolution with a logarithmic function compared with an exponential function $y = A \times [1 - \exp(-t/\tau)]$ suggests that the postseismic displacements close to the rupture are dominated by afterslip. The spatial pattern of the horizontal GNSS displacements resembles the coseismic deformation field (Figure 1d), which could result from either afterslip or viscoelastic relaxation.

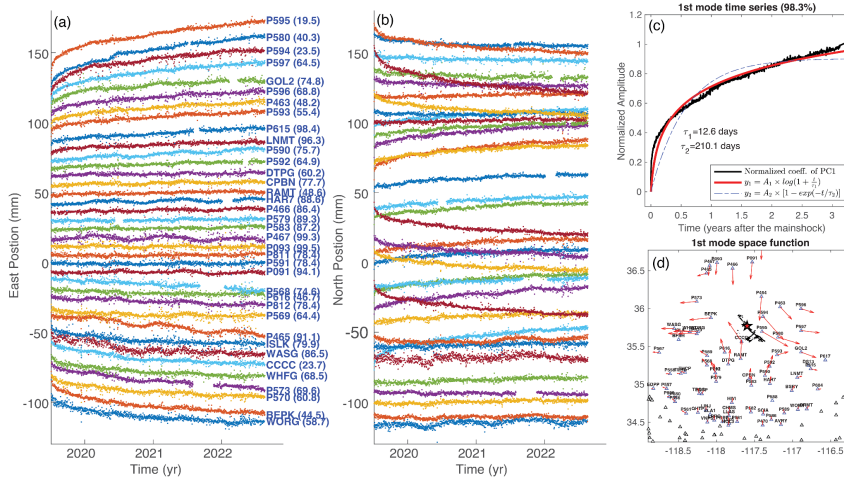


Figure 1. Postseismic displacement time series at GNSS stations within 100 km from the Mw 7.1 mainshock (a-b).

Numbers in parentheses of panel (a) denote the distance of the respective GNSS station to the epicenter of the mainshock in km. Panel (c) and (d) show the temporal and space functions of the first

principal component (PC1) of the postseismic GNSS displacement time series 3 years after mainshock.

Atmospheric perturbation remains one of the major error sources in InSAR measurement for low-magnitude surface deformation. In this project, we explored different approaches to mitigate the atmospheric noise when constructing the InSAR time series, including the methods based on numerical weather models (Jolivet et al., 2011), GNSS-based Zenithal Total Delay (ZTD) products (Yu et al., 2018), Common-Scene-Stacking (CSS) (Tymofeyeva et al., 2019), as well as a combination of them. The overall performance of the weather model correction is mixed, in that for some interferograms, it can indeed significantly reduce the phase variations, particularly at large scales, while for others the correction may deteriorate the results. This is largely because of the limited resolution of current weather models. For instance, the ERA-5 weather model used in this study has a spatial resolution of ~ 25 km and temporal resolution of 1 hour. The spatial resolution of modern SAR systems, on the other hand, is on the order of 10-100 meters. Interpolations in both space and time are therefore needed to obtain the path delay for each SAR pixel at the time of image acquisition. This may introduce large errors in the case of atmospheric conditions being highly dynamic. Continuous GNSS observations can provide high temporal resolution of ZTD products, but its poor spatial resolution, which is essentially determined by the average spacing of the GNSS network, still poses challenges to fully compensate for the atmospheric delay of a SAR image. Due to these limitations, the corrections with either ERA-5 weather model or GNSS ZTD products are shown to have limited performances. Specifically, the time series corrected with the ERA-5 weather model (pink squares in Figure 2c-d) or GNSS ZTD (green circles in Figure 2c-d) estimates both exhibit less scattering, compared to the one without any atmospheric noise correction (cyan diamonds in Figure 2c-d). However, they still contain large and rapid variations through time that cannot be easily associated with a postseismic relaxation process (Figure 2c-d). The CSS method, on the other hand, performing like a low-pass filter (e.g., Wang and Bürgmann, 2020), can effectively reduce the high-frequency noise in the temporal domain. Since the algorithm of CSS is based on the assumption that the atmospheric noise in SAR images is random in time, in the case where the atmospheric conditions exhibit systematic variations in time, e.g., seasonal variations, it is necessary to correct for the temporally correlated component before a CSS is applied. In this study, we find that combining the GNSS ZTD correction with CSS can effectively reduce the scattering in the time series, while still preserving the temporally decaying pattern expected from a postseismic relaxation process (green lines in Figures 2c-d).

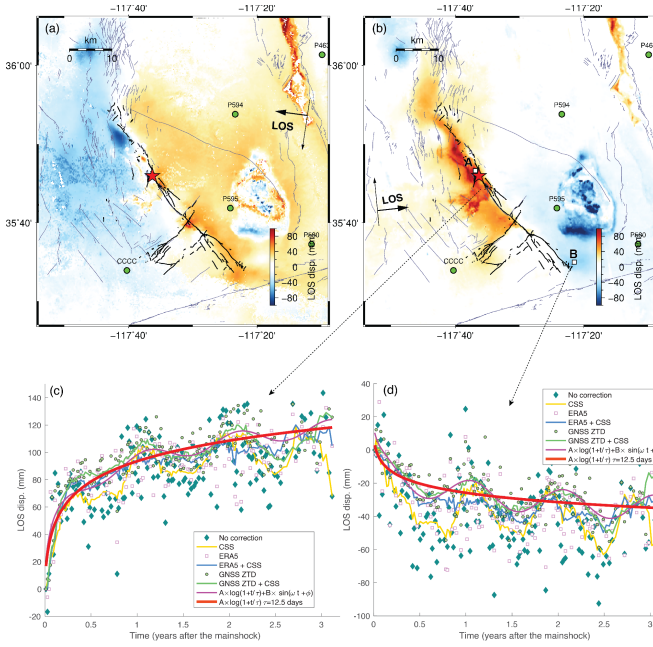


Figure 2. Postseismic line-of-sight (LOS) displacements derived from Sentinel-1 InSAR using data from the ascending track ASC64 (a) and descending tracking DES71 (b). Panels (c) and (d) show example line-of-sight (LOS) time series obtained with different approaches of atmospheric noise correction. Note that the LOS time series without atmospheric correction exhibit large scattering and apparent annual variation with a period of roughly 1 year, which is likely due to the seasonal variation of the tropospheric delay, as the amplitudes of such seasonal variation are significantly reduced when applying an atmospheric correction with either the ERA-5 weather model or the GNSS-based Zenith Total Delay products. The effect of the Common-

Scene-Stacking (CSS) (Tymofeyeva and Fialko, 2015) mainly reduces the high-frequency noise, and it preserves the relatively long-term deformation trend.

The resulting time series at each pixel is then fitted with a logarithmic function to estimate the cumulative displacement during a given time period. To reduce the uncertainties, we fix the relaxation time here to be the same value of 12.6 days estimated by fitting the first principal component (PC1) of the near-field GNSS time series (Figure 1c). The cumulative LOS displacements from both ascending and descending tracks 3 years after the mainshock are then combined to separate the horizontal and vertical displacement components (Figure 2). Since there are only LOS measurements from two look geometries, it is impossible to solve for the full 3D displacement component. Considering that the satellites fly along near-polar orbits, we assume that the ground motion along the north-south direction does not significantly contribute to the range changes, and only solve for the motion along the east-west and vertical directions. Similar to the GNSS observations, the horizontal component of the Sentinel-1 InSAR displacement field is characterized by mostly eastward motion on the eastern side of the mainshock rupture, and westward motion on the western side (Figure 2). The vertical component, however, is rather complicated, and mostly concentrated close to the rupture, particularly around the areas with fault geometry complexities. Some noticeable vertical deformation features include the uplift near the mainshock epicenter, where the fault strike changes direction to form a releasing bend, the fault junction between the Mw 6.4 foreshock and the Mw 7.1 mainshock ruptures, as well as the uplift and subsidence around the rupture tips. As is briefly discussed below, we suggest that the near-field vertical displacements observed by InSAR are mostly associated with poroelastic rebound in the shallow crust.

Results

Commonly considered postseismic relaxation mechanisms include continued aseismic afterslip on the fault, viscoelastic relaxation in the lower crust and upper mantle, poroelastic rebound in the water-bearing shallow crust, and shallow fault-zone dilatancy recovery (Bürgmann & Dresen, 2008; Fialko, 2004;

Fielding et al., 2009; Massonnet et al., 1996; Peltzer et al., 1998; Pollitz et al., 2000; Savage et al., 2003). For the sake of simplicity, in the current study, we accounted for the contribution of viscoelastic relaxation using an existing rheological model derived from modeling the postseismic deformation following the 1992 Landers and the 1999 Hector Mine earthquakes over a time period of two decades (Liu et al., 2020). The predicted surface displacements due to viscoelastic relaxation based on this rheological model were then subtracted from the postseismic GNSS and InSAR observations to explore the distribution of afterslip and properties of the shallow crust associated with poroelastic rebound. Although the horizontal component of the observed postseismic deformation in the relatively near field (<100 km) is qualitatively consistent with what one would expect from afterslip, the vertical deformation field appears to be best explained by poroelastic rebound. To avoid the potential bias due to poroelastic rebound, we only used the horizontal component of the postseismic displacements as shown in Figure 1-2 when inverting for the afterslip distribution. The resulting distribution of afterslip 3 years after the 2019 Ridgecrest mainshock is shown in Figure 3. The total moment release based on our preferred afterslip model is equivalent to an earthquake of $\sim M_w 6.52$, about 13 % of the coseismic moment release. Most of the afterslip is concentrated in a relatively shallow depth range above 25 km, and in areas of relatively low coseismic slip. This is in contrast to the afterslip model presented in Pollitz et al., (2021), where the major afterslip appears to be concentrated at a depth range well beneath the coseismic rupture area. Because for strike-slip faults, both viscoelastic relaxation and afterslip can give rise to similar patterns of surface deformation in the horizontal direction (Savage & Prescott, 2012), the inverted afterslip could be biased toward a deeper depth range, if the contribution from viscoelastic relaxation is not properly accounted for. Interestingly, the afterslip model presented in Pollitz et al. (2021) was based on a joint inversion for both the afterslip and viscoelastic relaxation. The large difference between our preferred afterslip shown in Figure 3 and that in Pollitz et al. (2021) once again highlights the uncertainty of using postseismic deformation to probe the rheological properties of the fault and host rocks.

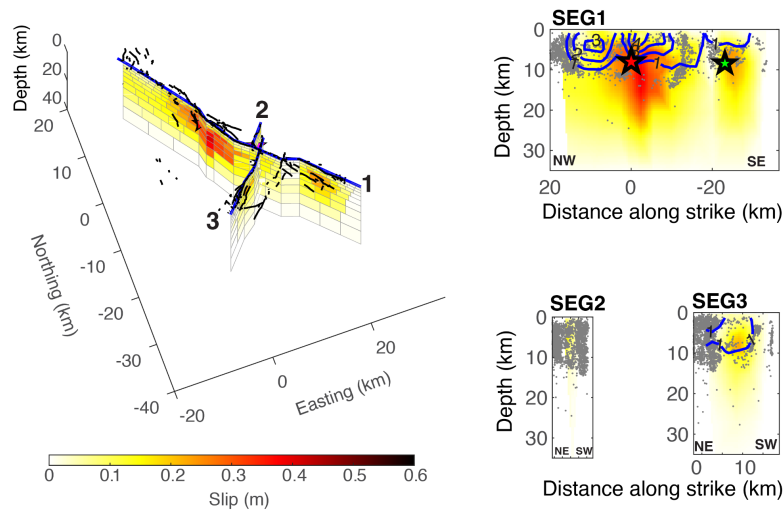


Figure 3. Distribution of afterslip 3 years after the 2019 Ridgecrest earthquake sequence. Blue lines in the right panels represent the contours of coseismic slip at an interval of 1 meter starting from 1 meter (Wang et al., 2020).

The resulting afterslip model fits well with the horizontal component of the InSAR and GNSS observations, but fails to match the pattern of the vertical component. Qualitative analysis suggests that the observed vertical displacement near the fault is mainly due to poroelastic rebound (Wang & Bürgmann, 2020). The temporal evolution of vertical deformation at locations that are likely due to poroelastic rebound

allows us to constrain the hydraulic diffusivity of the shallow crust. Particularly, we find that the uplift feature at the releasing bend of the mainshock epicenter can be well approximated by a poroelastic rebound model with a hydraulic diffusivity of $\sim 0.1 \text{ m/s}^2$ in the top 2 km .

Although the combined model including afterslip and viscoelastic relaxation based on the rheological model of Liu et al. (2020) can fit the GNSS displacement south of the rupture reasonably well, the model significantly underpredicts the GNSS displacements at stations to the north of the rupture. This indicates a lateral variation in the rheology across the region. We have also analyzed the GNSS data at even greater distances from the rupture. The results reveal robust transient deformation at stations across much of California (up to the latitude of $\sim 40^\circ\text{N}$) and western Nevada. The transient deformation at such a great distance is another manifestation of viscoelastic relaxation excited by the 2019 Ridgecrest earthquakes.

Another objective of this project is to explore the feasibility of using Multi-Aperture Interferometry (MAI) of Synthetic Aperture Radar (SAR) to image the tectonic motion along the satellite's flying direction, which has been of high priority for deriving a complete 3D displacement field using SAR data. We have tested the method with ALOS-2 ScanSAR data acquired over the Ridgecrest area using the InSAR Scientific Computing Environment (ISCE) software. The preliminary results show that, as expected, the MAI is much noisier compared to the conventional LOS InSAR. One major problem is that similar to the conventional InSAR, MAI also suffers from severe contamination due to ionospheric perturbation. The range split-spectrum method has proven to be an effective method correcting the ionospheric perturbations in conventional InSAR (Liang et al., 2017). However, the results show that even with the range-split spectrum method, many of the MAI interferograms we tested still exhibit large-scale variations that are possibly due to residual ionospheric noise. Additionally, the relatively small postseismic displacements are more difficult to measure accurately with MAI than the large coseismic measurements (Fielding et al., 2020). We are exploring how ionosphere correction can be applied more accurately in the MAI processing flow and different post-processing methods (e.g., filtering, stacking, deramping) to improve the MAI accuracy.

References

- Barbot, S., Fialko, Y., & Bock, Y. (2009). Postseismic deformation due to the M w 6.0 2004 Parkfield earthquake: Stress-driven creep on a fault with spatially variable rate-and-state friction parameters. *Journal of Geophysical Research*, 114(B7). <https://doi.org/10.1029/2008jb005748>
- Bürgmann, R., & Dresen, G. (2008). Rheology of the Lower Crust and Upper Mantle: Evidence from Rock Mechanics, Geodesy, and Field Observations. *Earth and Planetary Sciences*, 36(1), 531 – 567. <https://doi.org/10.1146/annurev.earth.36.031207.124326>
- Dong, D., Fang, P., Bock, Y., Webb, F., Prawirodirdjo, L., Kedar, S., & Jamason, P. (2006). Spatiotemporal filtering using principal component analysis and Karhunen–Loeve expansion approaches for regional GPS network analysis. *Journal of Geophysical Research: Solid Earth*, 111(B3). <https://doi.org/10.1029/2005jb003806>
- Fialko, Y. (2004). Evidence of fluid-filled upper crust from observations of postseismic deformation due to the 1992 Mw7.3 Landers earthquake. *Journal of Geophysical Research: Solid Earth*, 109(B8). <https://doi.org/10.1029/2004jb002985>
- Fielding, E. J., Lundgren, P. R., Bürgmann, R., & Funning, G. J. (2009). Shallow fault-zone dilatancy recovery after the 2003 Bam earthquake in Iran. *Nature*, 458(7234), 64 – 68. <https://doi.org/10.1038/nature07817>
- Fielding, E. J., Liu, Z., Stephenson, O. L., Zhong, M., Liang, C., Moore, A., Yun, S.-H. & Simons, M., 2020. Surface deformation related to the 2019 Mw 7.1 and 6.4 Ridgecrest Earthquakes in California from GPS, SAR interferometry, and SAR pixel offsets, *Seismol. Res. Lett.*, 91, 2035–2046. <https://doi.org/10.1785/0220190302>
- Jolivet, R., Grandin, R., Lasserre, C., Doin, M. -P., & Peltzer, G. (2011). Systematic InSAR tropospheric phase delay corrections from global meteorological reanalysis data. *Geophysical Research Letters*, 38(17), L17311. <https://doi.org/10.1029/2011gl048757>
- Liang, C., Fielding, E. J. & Huang, M.-H., 2017. Estimating Azimuth Offset With Double-Difference Interferometric Phase: The Effect of Azimuth FM Rate Error in Focusing, *IEEE Transactions on Geoscience and Remote Sensing*, 55, 7018–7031. <https://doi.org/10.1109/TGRS.2017.2737955>
- Liu, S., Shen, Z.-K., Bürgmann, R., & Jónsson, S. (2020). Thin crème brûlée

rheological structure for the Eastern California Shear Zone. *Geology*, 49(2), 216–221.
<https://doi.org/10.1130/g47729.1>

Massonnet, D., Thatcher, W., & Vadon, H. (1996). Detection of postseismic fault-zone collapse following the Landers earthquake. *Nature*, 382(6592), 612–616.
<https://doi.org/10.1038/382612a>

Peltzer, G., Rosen, P., Rogez, F., & Hudnut, K. (1998). Poroelastic rebound along the Landers 1992 earthquake surface rupture. *Journal of Geophysical Research: Solid Earth*, 103(B12), 30131–30145. <https://doi.org/10.1029/98jb02302>

Pollitz, F. F., Peltzer, G., & Bürgmann, R. (2000). Mobility of continental mantle: Evidence from postseismic geodetic observations following the 1992 Landers earthquake. *Journal of Geophysical Research: Solid Earth*, 105(B4), 8035–8054.
<https://doi.org/10.1029/1999jb900380>

Pollitz, F. F., Wicks, C. W., Svarc, J. L., Phillips, E., Brooks, B. A., Murray, M. H., & Turner, R. C. (2021). Postseismic Relaxation Following the 2019 Ridgecrest, California, Earthquake Sequence. *Bulletin of the Seismological Society of America*, 112(2), 734–749. <https://doi.org/10.1785/0120210170>

Savage, J. C., & Prescott, W. H. (2012). Asthenosphere readjustment and the earthquake cycle. *Journal of Geophysical Research*, 83(B7), 3369–3376.
<https://doi.org/10.1029/jb083ib07p03369>

Savage, J. C., Svarc, J. L., & Prescott, W. H. (2003). Near-field postseismic deformation associated with the 1992 Landers and 1999 Hector Mine, California, earthquakes. *Journal of Geophysical Research: Solid Earth*, 108(B9).
<https://doi.org/10.1029/2002jb002330>

Tymofeyeva, E., Fialko, Y., Jiang, J., Xu, X., Sandwell, D., Bilham, R., et al. (2019). Slow Slip Event On the Southern San Andreas Fault Triggered by the 2017 Mw8.2 Chiapas (Mexico) Earthquake. *Journal of Geophysical Research: Solid Earth*, 124(9), 9956–9975. <https://doi.org/10.1029/2018jb016765>

Wang, K., & Bürgmann, R. (2020). Co- and Early Postseismic Deformation Due to the 2019 Ridgecrest Earthquake Sequence Constrained by Sentinel-1 and COSMO-SkyMed SAR

Data. *Seismological Research Letters*, 91(4), 1998 – 2009.
<https://doi.org/10.1785/0220190299>

Wang, K., Dreger, D. S., Tinti, E., Bürgmann, R., & Taira, T. (2020). Rupture Process of the 2019 Ridgecrest, California Mw 6.4 Foreshock and Mw 7.1 Earthquake Constrained by Seismic and Geodetic Data. *Bulletin of the Seismological Society of America*, 110(4), 1603 – 1626. <https://doi.org/10.1785/0120200108>

Yu, C., Li, Z., Penna, N. T., & Crippa, P. (2018). Generic Atmospheric Correction Model for Interferometric Synthetic Aperture Radar Observations. *Journal of Geophysical Research: Solid Earth*, 123(10), 9202 – 9222.
<https://doi.org/10.1029/2017jb015305>